RSC Advances

PAPER

View Article Online
View Journal | View Issue

Cite this: *RSC Adv.*, 2023, **13**, 22007

Hollow nanostructured NiO particles as an efficient electrode material for lithium-ion energy storage properties †

Young Geun Hwang, Venugopal Nulu, Arunakumari Nulu and Keun Yong Sohn *

This work has developed a straightforward approach to obtaining NiO hollow structures by using Li_2O_2 as an easily removable template. The easy availability and electrochemically active nature of NiO have attracted researchers' attention as an anode electrode for Li-ion storage applications, including Li-ion secondary batteries (LIBs) and for Li-ion hybrid supercapacitors (LiHSCs; which offer higher power densities than LIBs without compromising energy density). However, NiO usage has been limited to its low reaction reversibility, poor conductivity, and conversion reaction capability. Recently, hollow nanostructured materials have attracted attention as efficient battery materials due to their fascinating structural features. This study presents a modified Li_2O_2-assisted method to obtain porous open 3D architectures of NiO nanostructures. The resultant hollow structures are electrochemically studied as an anode for a LIB, exhibiting excellent stability over hundreds of cycles. The result is recognized as one of the finest among NiO anodes reported. Also, NiO hollow structures studied as anodes for LiHSC devices fabricated with activated carbon cathodes exhibit an outstanding comprehensive electrochemical performance which is better than the typical LIB and supercapacitors.

Received 24th May 2023
Accepted 13th July 2023

DOI: 10.1039/d3ra03467d

rsc.li/rsc-advances

1 Introduction

Hollow nanostructures are a particular class of three-dimensional (3D) structures due to their high specific surface area, low density, excellent infusion, and shell permeability and are characterized by the size and shape of the level of nanoparticles, void size of the specific hollow particle (ranges between 10 or 100th of nanometer size) and lateral dimensions up to the few micrometer scale. With these structural features, these hollow structures have attracted researchers attention as battery electrode materials for enhancing the battery capacity and rate performance and also make them promising for applications in many fields such as photonic devices, drug delivery, nanocatalysts, and nanoreactors.[1–4] Among several metal oxides, NiO has received substantial consideration because of its easy availability, cost-effectiveness, and its abundance in nature and has represented a special class of materials in vast application fields, such as supercapacitors, battery cathodes and anodes, gas sensors, fuel cell electrodes, catalysts, absorbents and so forth.[5–8]

Many efforts have been devoted to the controlled synthesis of NiO hollow structures by various template-based physiochemical routes.[9–12] The templates employed included polystyrene spheres,[13] metal–organic framework,[14] and bio template.[15] However, organic templates needed special conditions to remove, the difficulty of handling, and special laboratory equipment to conduct experiments, thus limiting the large-scale applications. Alternatively, a simple synthesis approach is much essential to preparing hollow structures. NiO is one widely investigated conversion-type metal oxide anode material for lithium-ion secondary batteries (LIBs). Usually, like other metal oxides, NiO suffers from significant volume change coupled with intrinsically low ionic/electronic conductivity.[16] The solutions to overcome these issues are studying smaller-sized nanoparticles, such as various NiO nanostructures such as hollow spheres, nanofibers, and nanosheets, which have been studied as efficient anode electrodes for LIBs.[17–21] Given these benefits, NiO nanostructures can also be applicable as emerging anode material for the evolving hybrid storage LiHSC technology, which fits between LIBs and supercapacitors to deliver energy and power densities.[22] Using hollow nanostructures as electrode materials, could significantly improve the diffusion kinetics of lithium ions and the electron transport rate by enhancing the active electrode surface area and providing an electrode/electrolyte contacting reaction area that could progress the power and energy densities of the existing LiHSCs.

Department of Nanoscience and Engineering, Center for Nano Manufacturing, Inje University, 197 Inje-ro, Gimhae, Gyeongnam-do 50834, Republic of Korea. E-mail: ksohn@inje.ac.kr

† Electronic supplementary information (ESI) available: LIBs anode performance comparison graph with literature, EIS studies, TEM analysis, LiHSC cathode test. See DOI: https://doi.org/10.1039/d3ra03467d

We reported a chemical step followed by a low-temperature thermal oxidation method to fabricate NiO hollow structures with excellent electrochemical properties for LIBs. We have applied first-time Li_2O_2 as an easily removable template to prepare NiO hollow structures. The electrode delivered enhanced electrochemical properties than the bulk NiO particles, attributed to NiO particles' favorable porous hollow morphology.

2 Results and discussion

The phase of the h-NO and b-NO were determined using XRD, and the surface morphology of the h-NO was studied by SEM, respectively, as shown in Fig. 1. The X-ray diffraction patterns of the synthesized powders were indexed to the cubic NiO (PDF card no. 47-1049), as seen in Fig. 1a. No other impurity peaks were observed. The broad peaks observed in the XRD patterns of h-NO designate low crystallinity due to the presence of nano-sized particles. Fig. 1b shows the field emission scanning electron microscope (FESEM) images of h-NO (colored one in the inset), which contained disorderly combined thoroughly and partially formed open-mouth type hollow nanoparticles (size ranges from 100–300 nm). Fig. 1c shows the EDS elemental mapping of the h-NO sample, which indicates the presence of Ni and oxygen are well distributed within the sample. The extra carbon and platinum peaks are obtained from the carbon tape substrate which was used for the powder loading and from the platinum sputtering that was done before SEM analysis, thus, the carbon and platinum contents are not taken into consideration in the final result of the elemental analysis. The partially molded individual nanoparticles are shown in the SEM images (Fig. 1b and d), where the porous hollow interiors with a uniform shell thickness ranging from 30 to 50 nm and the outer surface of each particle are composed of numerous nanoparticles with a particle size of about ~10–20 nm. The aggregated arrays of hollow particles are displayed in Fig. S1a.† The beautiful arrangements of partially open heart-like hollow particles are shown in Fig. S1b† (marked with arrows). Interestingly, each hollow particle is accompanied by well-defined arrays of nanoparticles interconnected, leaving some nano-sized spaces between them. Fig. 1d shows the corresponding energy-dispersive X-ray spectroscopy (EDX) map of h-NO, which shows the existence and uniform distribution of Ni, and O elements with appropriate amounts of elemental atomic percentage, as shown in the inset table of Fig. 1c. Also, an extra XRD analysis was performed to distinguish the phase of the obtained powder before heat treatment, and the result revealed the formation of α-$Ni(OH)_2$ (see Fig. S2†).

Fig. 2a shows the TEM image of the h-NO sample, which contains hollow morphology with randomly arranged crystalline nanoflakes with meso/nanoscale voids. The SAED pattern in Fig. 2b, measured on the marked region (colored circle) in Fig. 2a, is different from the polycrystalline nature of the outer shell of the particular hollow particle; the patterns match well

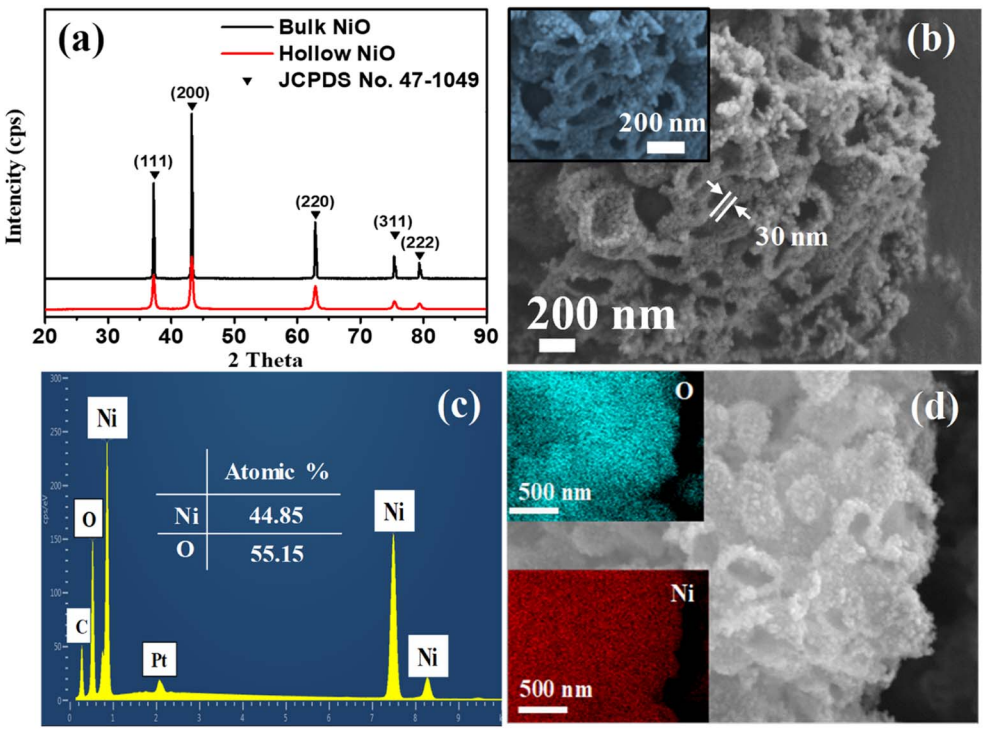

Fig. 1 (a) XRD patterns of the hollow porous NiO (h-NO) and bulk NiO (b-NO). (b) SEM image of accumulated aggregates of h-NO three-dimensional hollow nanoparticles self-assembled to microbundles and the colored inset shows its corresponding close view of the mini group of hollow particles captured at a specific location in image (b). (c and d) SEM-EDX of the h-NO shows successfully prepared NiO hollow particles with carbon and platinum peaks obtained from carbon tape substrate and platinum sputtering before checking SEM (carbon and platinum contents are not counted).

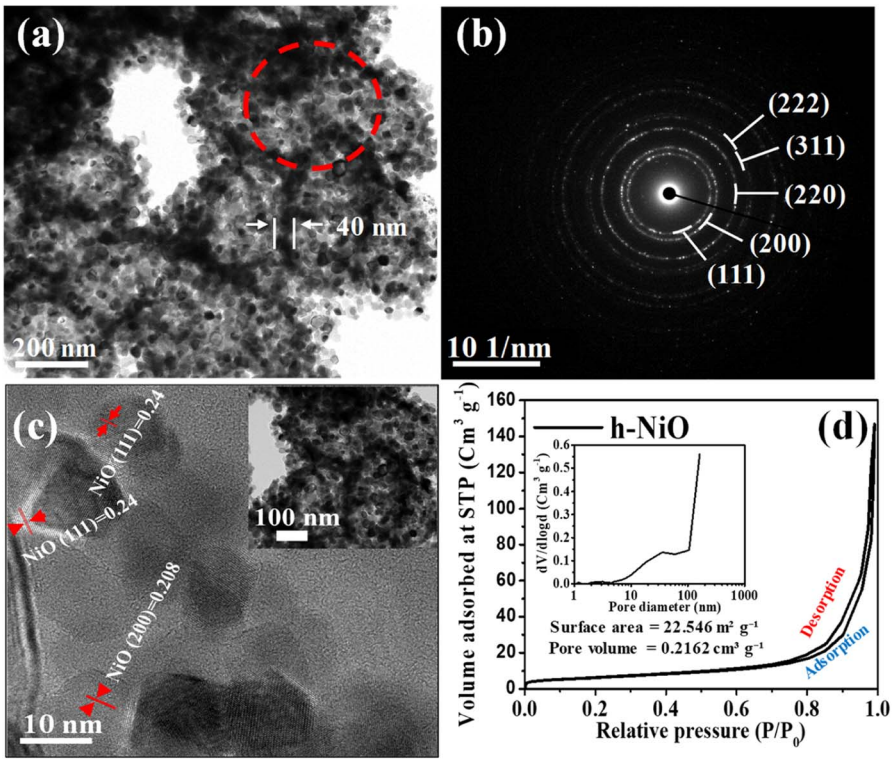

Fig. 2 (a) HRTEM images of h-NO hollow particles; marked wall thickness of about 40 nm for a specific hollow particle escorted with porous nature. (b) SAED pattern of the respective red color selected region is shown in (a). (c) HRTEM image of the selected area in the hollow particles shown in the inset image indicates the well-resolved lattice fringes corresponding to the NiO lattice planes (d) N_2 adsorption–desorption isotherms of the h-NO (inset: pore size distribution of the h-NO sample).

with the XRD result.[23] Fig. 2c is a magnified HRTEM view of the randomly arranged NiO nanoparticles of the specific hollow particle (from the right inset image of Fig. 2c), reveals the high crystalline nature of interconnected porous NiO particles and specifies that the well-resolved lattice fringes with an interplanar spacing of 0.21 and 0.24 nm correspond to the (200) and (111) lattices planes of the NiO rock salt structure, respectively. These results are supported by the XRD characterization (shown in Fig. 1a).

Fig. 2d depicts the BJH isotherms of h-NO. The isotherms of these samples revealed the presence of initial nitrogen uptake at low relative pressure P/P_0 ($\leq$0.7), which is attributed to the fact of small number of nanopores. The type IV hysteresis loop was observed from 0.7–0.9, and it was seen above 0.8, indicating that the meso/nanopores are inter-crystalline pores due to nanocrystals' aggregation.[24] The pore size distributions of h-NO show wide mesopores between 10 and 100 nm pores (as shown in the inset). The obtained BET-specific surface area was 22 $m^2\ g^{-1}$ with a pore volume of 0.2162 $cm^3\ g^{-1}$, respectively. The extra nanopores' presence enhanced the sample's resultant surface area.

X-ray photoelectron spectroscopy (XPS) was performed for fresh samples of h-NO, and the resultant plots are shown in Fig. 3. The survey spectrum of h-NO is depicted in Fig. 3a, which reveals the presence of Ni and O. Ni 2p spectrum shown in Fig. 3b edge splits by spin–orbital coupling the prominent peak at ~854 eV (satellite peak at ~861 eV) and $2p_{1/2}$ central mountain at ~872 eV with its satellite peak at ~879 eV, which are consistent with the NiO phase.[25] The other minor peaks at 852 and 870.04 eV should be attributed to the low content of Ni_2O_3, but since the phase is not detected in XRD, we expect that to be negligible.[25] Concerning the O1s spectrum in Fig. 3c, the peaks observed at the 529.6 eV originated from NiO, while the other peak at 531.51 eV corresponds to the Ni_2O_3.[26]

The results confirmed that our method is a facile approach to getting NiO hollow particles (reaction pathway shown in Fig. 4). The expected reaction path is expected to be started with a slow neutralization reaction between Li_2O_2 particles and nitrate ions of $Ni(NO_3)_2 \cdot 6H_2O$, which leads to oxygen evolution during the reaction was utilized to oxidize the Ni(II) cations to α-$Ni(OH)_2$ and expecting the possibility of NiO_x phase formation in minor limited amounts (data not shown). In the *in situ* generated α-$Ni(OH)_2$ precipitate primary layer encapsulated Li_2O_2 particles, the nucleation proceeds up to a certain thickness towards the right angle direction of the host Li_2O_2 surface. Simultaneously, the Li_2O_2 particle consumes by reacting with the remaining free $(NO_3)^-$ ions by leaving void spaces within the solid aggregated $Ni(OH)_2/Li_2O_2$ particles. Li_2O_2 particles are consumed and left behind semi-formed $Ni(OH)_2/NiO_x$ hollow regions. After being washed with water and dried at room temperature, we measured XRD, and the resultant sample showed α-$Ni(OH)_2$ phase (see Fig. S2†), and we hardly found the

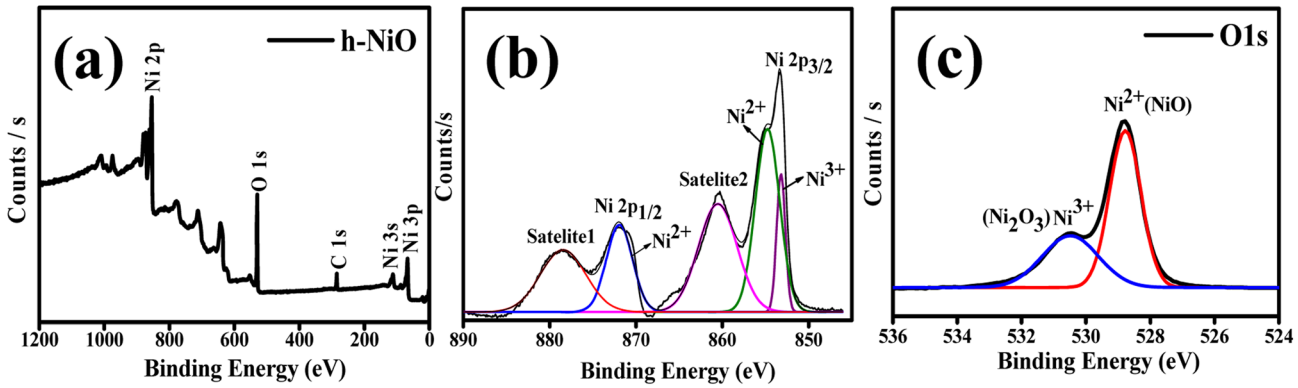

Fig. 3 XPS spectrograms for hollow NiO (h-NO), (a) XPS survey scan, (b) Ni2p, and (c) O1s.

NiO_x phase, so in Fig. 4, we considered only α-$Ni(OH)_2$. Untreated Li_2O_2 particles are wholly dissolved after washing with water and alcohol[27] and then subjected to annealing at 500 °C, resulting in black-colored powder with hollow particles of the NiO phase.

The prepared h-NO and b-NO electrodes are tested initially as anodes for LIBs. The electrochemical cyclability and corresponding charge–discharge profiles of h-NO and b-NO are shown in Fig. 5a and b. From Fig. 5a, the h-NO electrode exhibited high discharge capacities of 706 mA h g^{-1} for the fourth cycle and gradually increased and stabilized at about 852 mA h g^{-1} after 50 cycles with 70.3% of initial coulombic efficiency (ICE) for the first cycle and is steadily stabilized at 99.2% after 50 cycles. While, the discharge capacities of the b-NO electrode were relatively lower than that of h-NO (*i.e.*, 554 mA h g^{-1} for the fourth cycle and stabilized at 529 mA h g^{-1} after 50th cycles; 60.2% of ICE for the 1st cycle and is stabilized at 99.1%, respectively). The corresponding voltage *vs.* specific capacity charge–discharge profiles for the 1st, 2nd, and 50th cycles for the h-NiO electrode are shown in Fig. 5b. The wide voltage plateau at about 0.54 V is followed by a sloping curve during the first discharge and the discharge plateau shifts to around 1.4 V for the successive consecutive cycles in the subsequent discharge process whereas the charge plateau is kept at about 2.2 V. These profiles are matched well with the reported NiO anode electrodes.[28] Fig. 5c shows the cyclic voltammograms (CVs) for the h-NO electrode. A strong cathodic peak is located in the first cathodic scan at 0.23 V, which corresponds to the initial reduction of NiO to Ni and the formation of amorphous Li_2O alongside a solid electrolyte interface (SEI).[28] The two typical small peaks at the anode side are observed at 1.3 and 2.2 V, consistent with the reductions corresponding to the NiO formation and Li_2O decomposition.[26] The peaks shifted to 1.5 and 2.3 V from the third cycle for the subsequent cycles due to structural or textural modifications.[29] The rate performance of both electrodes is shown in Fig. 5d and it is clear that the h-NO electrode shows much higher capacities at different applied current densities than the b-NO electrode. The h-NO electrode shows specific capacities for every fourth cycle measured at current densities of 100, 200, 400, 800, 1600, and 3200 mA g^{-1} are 887, 851, 790, 701, 471, and 298 mA h g^{-1}, respectively, which are higher than those of b-NO (576, 516, 439, 377, 237 and 123 mA h g^{-1} at current densities of 100, 200, 800, 1600, and 3200 mA g^{-1}, respectively). The hollow structured feature of NiO is responsible for the efficient performance of the electrode, particularly at high current rates, which, in turn,

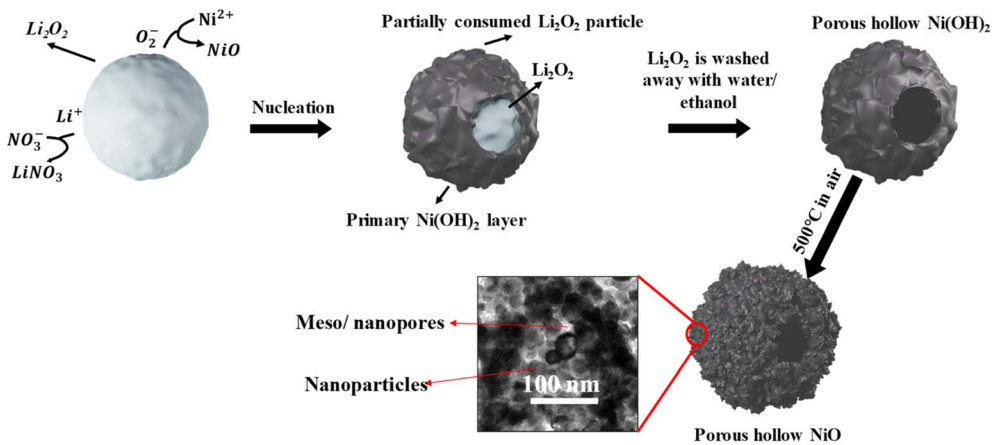

Fig. 4 Schematic illustration of the prepared NiO porous hollow particles.

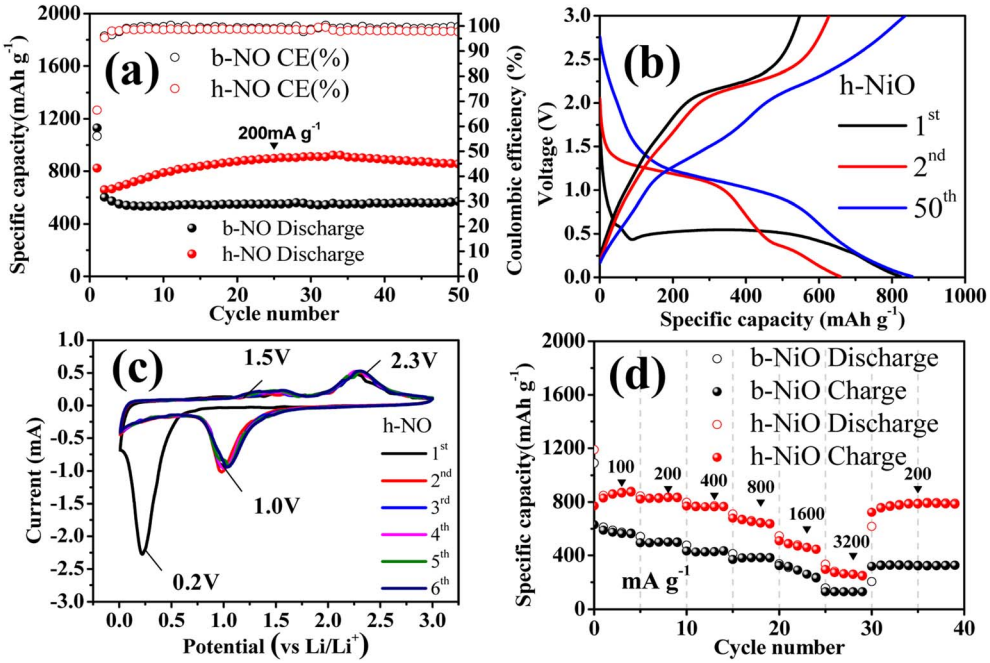

Fig. 5 Electrochemical characterization of h-NO and b-NO. (a) Cycle performance with coulombic efficiency at 200 mA g^{-1} and their respective charge–discharge voltage profiles for the 1st, 2nd, and 50th cycles are shown in (b). (c) Cyclic voltammograms for the first six cycles of h-NO with a scan rate of 0.1 mV s^{-1}. (d) Rate performances of the h-NO and b-NO at different current densities.

stand as one of the best in recent times among the reported results from other studies on different nanostructured NiO anodes for LIBs[13,14,16–18] (see Fig. S3 in ESI†). The EIS testing was carried out for the freshly prepared h-NO and b-NO electrodes to further understand. The Nyquist plot of both electrodes represents semicircles from the high to the medium-frequency region and an inclined line represents the low-frequency region (as seen in Fig. S4†). The semicircle diameter corresponds to the Li-ion migration (*i.e.*, charge transfer resistance, R_{ct}), and the slope of the inclined line replicates the Li-ion diffusion resistance in the solid electrode active material.[30] Among both electrodes, the h-NO reflects a significantly lower R_{ct} (124 Ω) value than the b-NO (209 Ω), showing that hollow structures can effectively increase the transfer of electrons and surface charges that can enhance the electrochemical performance of the electrode material. But, h-NO has a lower slope, indicating higher diffusion kinetics than the b-NO electrode.

Moreover, the morphology and structure of the h-NO electrode after 50 cycles are observed by TEM and HRTEM, and the micrographs are shown in Fig. S5.† As shown in images a and b of Fig. S5,† the structural deformation of the specific NiO hollow particle is seen in Fig. S5a.† Still, the porous nature is persistently reserved after 50 cycles (see red small colored circles in Fig. S5b†) alongside aggregation of ultrafine nanograins, which can provide easily accessible channels for lithium-ion diffusion and relieve the volume changes of the NiO.

To better realize the NiO (h-NO) reaction behavior with Li^+ ion and to understand the formation of any secondary phase on the NiO surface, the h-NO electrode was cycled 50 times to let the sizeable secondary phase gather onto the surface. The resulting species were surveyed by XPS (shown in Fig. 6a).

In Fig. 6b, deconvoluted by Gaussian curves and the XPS spectrum comprised two regions representing Ni $2p_{3/2}$ (850–860 eV) and Ni $2p_{1/2}$ (870–880 eV) spin–orbit levels. The Ni 2p spectra display consists of prominent peaks of Ni $2p_{3/2}$ and Ni $2p_{1/2}$ at binding energies 854.52 and 871.76 eV, and their broad corresponding shake-up satellite peaks are located at 861.72 and 879.16 eV respectively. The noticeable energy separation between Ni $2p_{3/2}$ and Ni $2p_{1/2}$ is about 17.4 eV, which corresponds to the oxidation state of Ni^{2+} and confirms the formation of the NiO phase as per the previous report.[31] Whereas the other Ni_2O_3 minor peaks observed at 852 and 870.04 eV before cycled electrode (see in Fig. 3b) have become very narrow and shifted to higher binding energies (suggests higher oxidation states), indicating the reduced content of Ni_2O_3 on the outer surface of the electrode and should be attributed to the negligible content. As shown in Fig. 6c, after intensive 50 cycles, the two different intensity O1s peaks shown in Fig. 3c are extruded into a single central O1s peak at ~531.6 eV shifts a little to the higher level, indicating the change in the coordinating configuration of Ni–O, which could be due to the formation of (Ni^{2+}, Ni^{3+})–O. The O1s central peak noticed around 531.2–531.8 eV is due to the surface adsorbed oxygen species; the increase in the intensity of this peak implies that more adsorbed oxygen species are developed on the surface obtained from the created carbonates that are produced during the formation of the SEI layer. We believe that the higher oxygen species obtained from electrolyte decomposition products on the surface that are noticed in O1s spectra may generate local stoichiometry surface

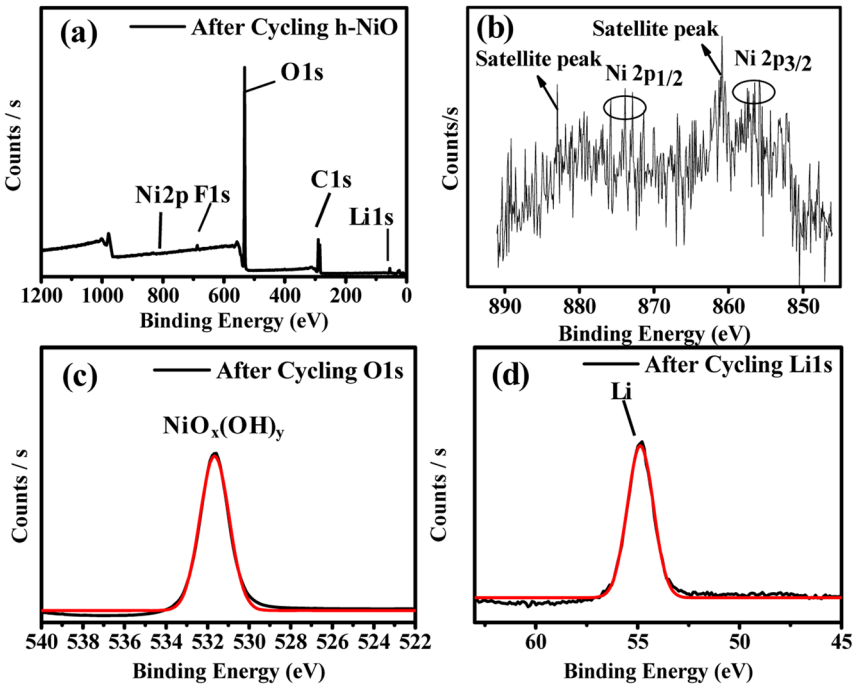

Fig. 6 XPS spectrograms for h-NO electrode after 50 charge–discharge cycles at 200 mA g^{-1}(a) survey spectrum. high-resolution scan of (b) Ni 2p (c) O1s (d) Li 1s.

reduction that favors minor contents of Ni_2O_3 to NiO conversion, as one would expect this could be the predominant pathway. This outcome indicates the NiO formation at the electrode's outer surface as the possible extruded Ni oxide phase after the Li-ion reaction.[32,33] The response of lithium-ions with NiO electrode can be summarized as follows:

$$NiO + 2Li^+ + 2e^- \leftrightarrow Ni^0 + Li_2O \quad (1)$$

$$2Li \leftrightarrow 2Li^+ + 2e^- \quad (2)$$

$$NiO + 2Li \leftrightarrow Ni^0 + Li_2O \quad (3)$$

For Li1s spectra (see Fig. 6d), the broad peak at 55.02 eV can be allotted to $LiOH/Li_2CO_3$ (~55.0 eV), Li_2O (~55.6 eV), and LiCOR (54.5 eV), generally observed from the SEI film composition.[34,35]

For more insight into the electrode transfer kinetics, we carried out the EIS experiment for cycled h-NO, and b-NO electrodes were measured within a frequency range of 10 mHz to 10 kHz (*vs.* Li/Li^+) and at an amplitude of 5 mV amplitude (see Fig. S6†). Fig. S6† shows the Nyquist plots of the electrodes after 50 charge–discharge cycles at 200 mA g^{-1} of both the electrodes and the equivalent circuit model as shown in the inset. The proposed circuit has the solution resistance (R_s), SEI layer resistance (R_{SEI}), charge transfer resistance (R_{ct}), two constant phase elements (CPE), and Warburg impedance (W_b) as parameters and is simulated by ZSimpWin software. It is observed that the R_{ct} value of h-NO is twofold lesser than the b-NO, and it could be due to the porous nanosized hollow particles' morphological features allowing fast Li-ion kinetics than the bulk particles during Li^+ reactions with the anode materials. The summarized R_s, R_{SEI}, and R_{ct} values are shown in Table 1S.†

Based on the CV and XPS (see Fig. 5c and 6) results, the most likely pathway for the solid-state conversion reaction of the NiO is illustrated in Fig. 7, where we assume that after 50 subsequent cycles, the primary (NiO) and a small amount of secondary phase (Ni_2O_3) were appeared on the hollow particle's outer surface layers along with minor Li_2O particles and the expected final side product of Li. Here our attempt to gain insight into the possible NiO phase formation in the literature during the conversion of NiO and Ni_2O_3 lithiation/delithiation reaction has been found, offering new ways to understand the metal oxides anode electrode chemistry. We proposed an expected possible lithium reaction pathway for the small quantity of Ni_2O_3 that appeared in the h-NO sample (confirmed from XPS results in Fig. 3b and 6b) in the below mechanism study and no further data was provided for the negligible amount of Ni_2O_3.

A hybrid technology of Li-ion hybrid supercapacitors was developed by integrating EDLC-based supercapacitors cathode and LIB anode components into one energy storage device is an efficient approach to enhance energy density by preserving high power density, which is concerned with extensive research attention.[36–40] The electrochemical performance of the AC cathode half-cells is shown in Fig. S7† at 100 mA g^{-1}. All half-cells displayed stable cycle life with specific capacities between 20–80 mA h g^{-1} (see Fig. S7a†). The AC cells cycled within the voltage ranges of 2–4.5 and 1–4 V delivered better specific capacities of about 60 mA h g^{-1} after 50 charge–discharge cycles. Their respective first three galvanostatic charge–discharge curves are shown in Fig. S7b and c.† Stable cycle life, together with the linear correlation of the discharged

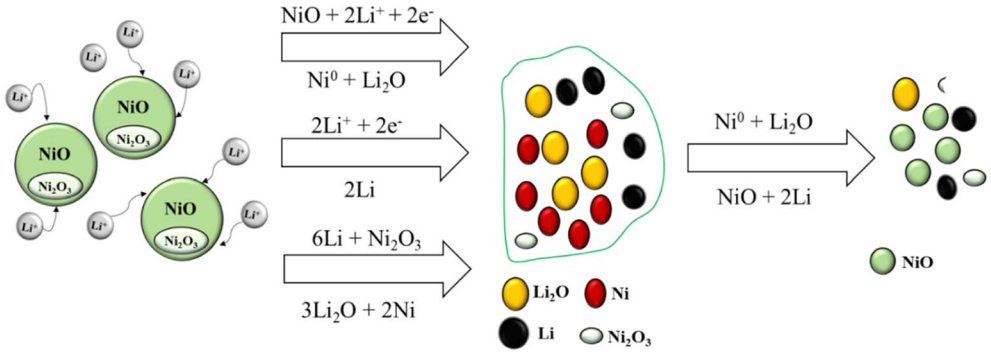

Fig. 7 A predicted mechanism for the solid-state conversion reaction of NiO.

curves of the AC cells, is due to the inherent non-faradic capacitive properties of the AC cathode. For asymmetric LiHSC, the h-NO anode and AC cathode half-cell analysis displayed stable operating discharge profiles in the potential windows of 0.1–1 V and 2–4 V (*vs.* Li/Li^+), respectively. Therefore, we have tested LiHSC cells within the voltage windows of 1–3.5, 1–4.5, and 1–4.2 V for initial cycles, and we have selected the best-performed potential of 1–4.2 V, which would cover the total working range of both electrodes. We optimized the n/p ratio and tested it at different voltage ranges in the LiHSC cells to reach the best electrochemical performance. To verify the optimized n/p ratio for the h-NO//AC LiHSC cell, three cells were assembled with n/p ratios of 0.60, 1.38, and 2.08 and tested within the voltage range of 1–4 V. Fig. S8† shows their respective energy *vs.* power density performance. The cell with n/p ratio of 1.38 delivered better performance than the other two cells with good energy and power density values. Therefore, we considered the same n/p balance for further studies. The rate performance of the h-NO//AC, LiHSC cell was displayed in Fig. 8a; we can see that the cell exhibited stable high capacities of 80 mA h g^{-1} at 0.1 A g^{-1} (based on the proportions of the active materials); close to 40 and 20 mA h g^{-1} even at high applied currents of 5 and 10 A g^{-1}, respectively. It is an excellent noted rate capability performance and remains stable cycling at different rates. The voltage *vs.* capacity plots at different current densities were measured and displayed in Fig. 8b. At 0.1–0.5 A g^{-1}, the middle section of the charge profiles was curved, which was due to the lithium-ions insertion and extraction mechanism; at and above 1 A g^{-1}, the curve shape was transformed into a linear line with triangular symmetry was exhibited, this is attributed to the capacitor characteristic. Further, no significant IR drop was noticed in these curves, which denotes the low-internal resistance of the system. The high-rate applications, including electric vehicles, space applications, elevators, and energy storage devices would remain able to endure repeated charge/discharge cycles with stable capacities. To this end, we tested the cyclic performance of h-NO//AC LiHSC at a higher current density (5 A g^{-1}; see Fig. 8c). The h-NO//AC hybrid cell demonstrated excellent cyclability for over 10 000 charge–discharge cycles with stable specific capacities of about 40 mA h g^{-1}. The capacity retention of h-NO//AC LiHSC is as high as 95.2% after 1000 cycles and 91.9% after 10 000 cycles, with the coulombic efficiency close to unity, and we noted that our LiHSC could complete fast charge–discharge within the 30 s at 10 A g^{-1} (see Fig. 8b) that is comparable with that of SCs. The cycling profile curves were shown in Fig. 8d. A minor decline in cycling capacity is likely caused by the battery-type anode, which may undergo volume changes during the charge–discharge process. However, it is worth noting that this cycling life is better than most reported LIC devices (see Fig. 9a). Ragone plots of the h-NO//AC, LiHSC hybrid device with an n/p ratio of 1.38 is illustrated in Fig. 9a, which can deliver an energy density of 253.0–85.0 W h kg^{-1} for power densities from 0.185 to 11.2 kW kg^{-1}. The maximum power density achieved by our cell is 5.18 kW kg^{-1} by maintaining the energy density of 126 W h kg^{-1}, which is a suitable requirement for future EVs. The Comparison between h-NO//AC and the reported excellent Li-ion hybrid capacitors developed from powder-based anodes and cathodes is shown in Fig. 9b.[41–45] The distinguished combination of energy-power densities delivered from our hybrid device is great compared with that of others. Our device maintained a high energy density higher than LIBs and sustained a high power density superior to typical AC//AC supercapacitors (see Fig. 9c),[46] which states its exceptional application projections.

The excellent hybrid cell performance of our developed h-NiO//AC system in terms of delivering great reversible capacities, stable cycling life, and outstanding rate performance, with an even-handed active electrode weight of ~4% respective to the total cell weight (excluding cell components weight), is a considerably lower content than the conventional packaged cell.[47–49] Still, the great performance is credited to the low-density, high-performance hollow structured h-NO anode and can be beneficial for designing lightweight smaller-size efficient energy storage devices. Consequently, our h-NiO//AC LiHSC device delivered excellent energy and power densities. The porous hollow structures of the h-NiO contributed to most of our device performance due to the extraordinary surface properties and interconnected hollow particle framework to endure the strain produced by the volume changes of the NiO anode electrode. Finally, the ultrafine NiO nanoparticles (~10–20 nm) framework arranged as the meso/nanoporous walls of each hollow particle (~200–400 nm) could increase the electronic conductivity and impede the aggregation of particles during cycling and make it an auspicious candidate for advanced Li-ion hybrid technology.

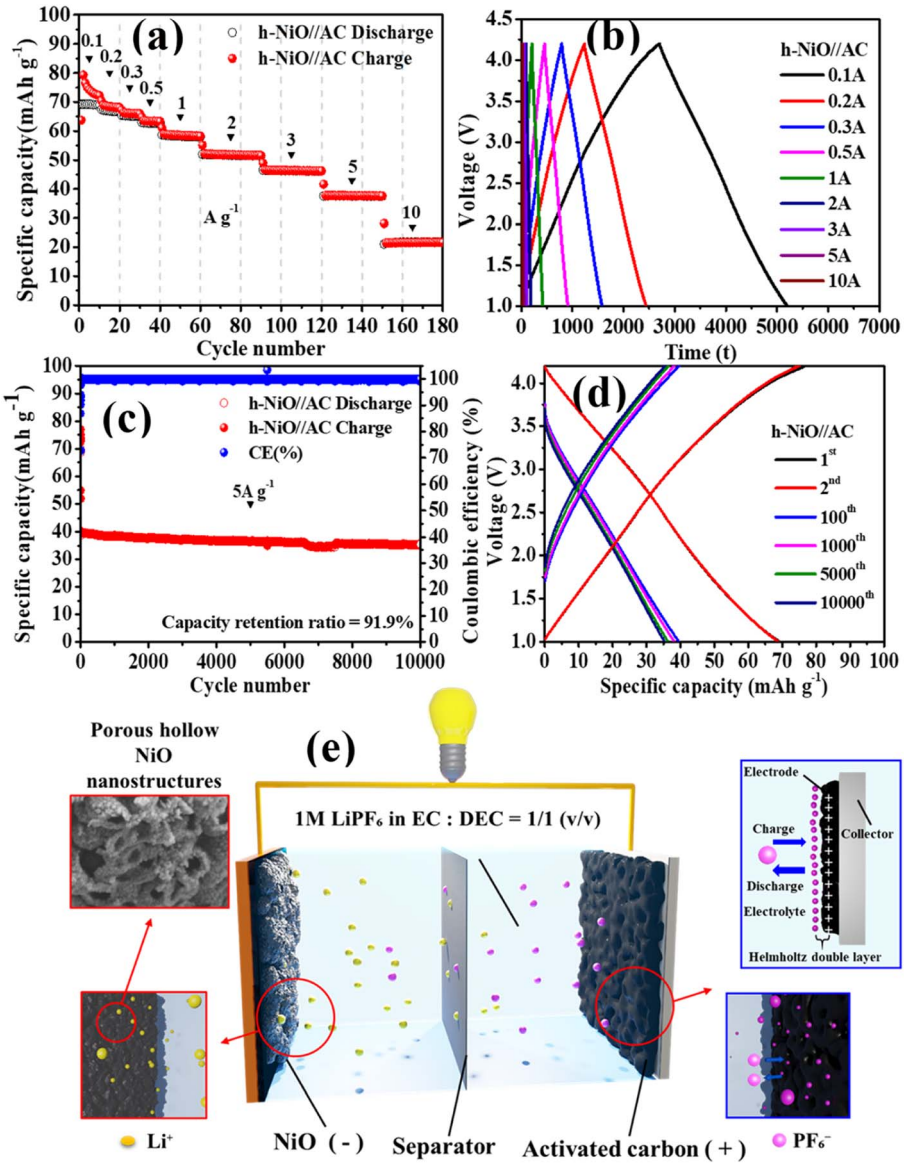

Fig. 8 The electrochemical performance of h-NO//AC LiHSC cell (a) rate capability was tested at various current densities. (b) The galvanostatic charge–discharge curves in the 1–4.2 V voltage range correspond to (a). (c) Cycling performance at 5 A g^{-1} (d) charge–discharge curves of the h-NO//AC LiHSC cell cycled in (c). (e) Schematic illustration of h-NO//AC LiHSC device.

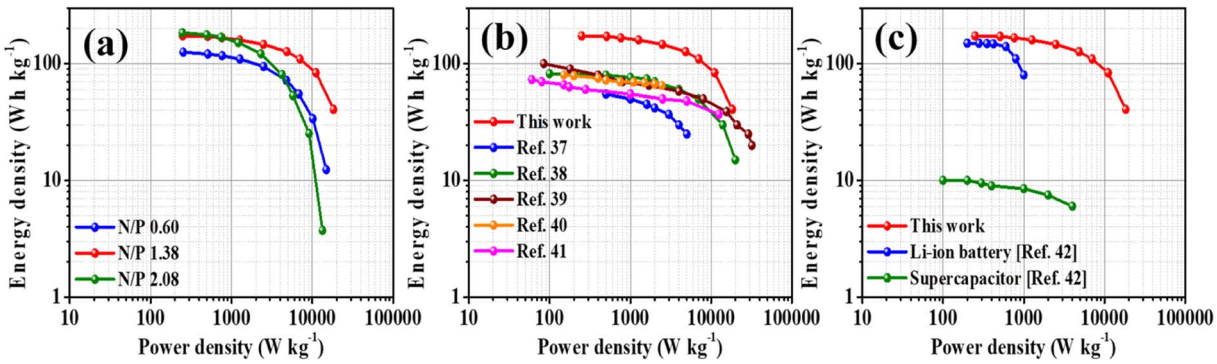

Fig. 9 Ragone plots comparison between (a) LiHSC cells assembled with different n/p ratios. (b) Our LiHSC cell *vs.* the reported Li-ion hybrid capacitors fabricated by different powder-based electrode materials and with (c) typical Li-ion battery and supercapacitor.

3 Conclusion

In conclusion, hollow NiO nanostructures are successfully prepared by the modified simple chemical method mediated by Li_2O_2 as an easy water-washable template followed by annealing treatment. The obtained intertwined hollow particle sizes are in the nanometer range and outfitted with nanoflakes with nanoscale thick walls. As a result, the obtained hollow structures of NiO resulted in a highly capable LIB anode with excellent capacities of more than 800 mA h g^{-1} (which is still above the theoretical value) at high current rates (1600 and 3200 mA g^{-1}) over hundreds of cycles, which is comparable with the best among the NiO anodes for LIBs reported in previous studies. We can easily extend the synthesis method to other metal oxides, which can be helpful in developing fascinating materials for next-generation battery systems.

Further, we present an XPS investigation on the NiO conversion reaction with lithium-ions, which showed the presence of NiO as a major final product along with Li_2O and the low contents of Ni_2O_3. The fascinating surface characteristics including the well-interconnected NiO nanoparticles framework of each hollow particle leaving a meso/nanoporous space in between them can form ion-buffering reservoirs that can produce an active material that is capable to sustain high capacities with stable cycle performance at high current rates, representing one of the best NiO materials reported in the literature to date for LIBs.

The LiHSC cell fabricated from hollow NiO anode and activated carbon cathode delivers an energy density of 253 W h kg^{-1}, with a remarkable power density of 11.2 kW kg^{-1} accomplished at 85 W h kg^{-1}, and sustained sensible lengthy cycling stability with 91.9% capacity retention after 10 000 cycles. Our developed synthesis method here for the hollow NiO particles can explore a new area of research pathways, including developing new nanostructured hollow materials from other materials, prominent to the progress of advanced electrode materials for Li-ion storage applications that advanced energy storage devices including Li-ion hybrid supercapbattery, suitable for electric vehicles and future portable electronics.

4 Experimental

4.1 Synthesis method

$Ni(NO_3)_2 \cdot 6H_2O$ (0.069 M, Aldrich) solution was prepared by dissolving in isopropanol (100 mL). Then, Li_2O_2 (0.6 g, Aldrich) was added to the solution while stirring at room temperature. Initially, a light green color precipitate was formed, and after one h, the color of the solution remained the same. The reaction mixture was then kept under ambient conditions overnight while continuously stirred. The resultant residue was separated by centrifugation, then washed with deionized water and ethanol several times, and overnight dried at room temperature. The obtained powder was then subjected to heat treatment at 500 °C for one hour in the air resulting in black color powder. For comparison, bulk NiO powder was commercially purchased from viable sources. Hereafter, bulk NiO's and synthesized porous hollow structures of NiO are represented as b-NO and h-NO, respectively.

4.2 Material characterization

The surface morphologies of the h-NO and b-NO were determined using scanning electron microscopy (SEM, JSM7000F) and high-resolution transmission electron microscopy (HR-TEM, JEM-2100F). The phase and crystalline structure of the materials were analyzed using powder X-ray diffraction (XRD) with a Rigaku D/MAX-2200 Ultima instrument equipped with Cu Kα radiation ($\lambda = 1.54056$ Å) in the range of $10° < 2\theta < 80°$ operating at 30 kV and 40 mA. The surface area, pore volume, and pore diameter of the prepared materials were estimated following the Brunauer–Emmett–Teller (BET) and Barrett–Joyner–Halenda (BJH) methods. X-ray photoelectron spectroscopy (XPS, Thermo ESCALAB250xi) was used to detect the chemical states of Ni and O.

4.3 Electrochemical measurements

The working electrode for LIB was prepared by mixing the active material, a conductive additive (Super-P), and a polymer binder (polyamide-imide) (PAI) dissolved in *N*-methyl pyrrolidone (NMP), in a weight ratio of 70 : 15 : 15, respectively. Using the traditional doctor blade technique, the slurry was mixed with a mini ball mill and coated uniformly on Cu foil. After that, the coated Cu foil was dried at 80 °C for 3 h in air and further dried at 200 °C for 3 h in a vacuum oven. The active material loading on each electrode was typically 1–1.5 mg cm^{-2}. The prepared electrodes were assembled into 2032R-type coin cells using metallic lithium foil as the counter electrode, a Celgard 2300 membrane as a separator, and 1 M $LiPF_6$ in a 1 : 1 mixture of ethylene carbonate and diethyl carbonate as the electrolyte. The galvanostatic charge/discharge experiment was carried out using a BioLogic battery cycler at different current densities in 50–5000 mA g^{-1} with a cutoff voltage in the range of 0.01–3.0 V *vs.* Li/Li^+ under ambient conditions. Cyclic voltammetry (CV) experiments were performed using a Biologic VSP 300 at the same cutoff voltage at a scan rate of 0.1 mV s^{-1}. Electrochemical impedance spectroscopy (EIS) measurements were carried out with the same device in the frequency range of 10 kHz to 10 MHz with an alternating-current voltage of 5 mV.

Author contributions

Conceptualization, V. N.; methodology, V. N. and Y. G. H.; measurement and analysis, Y. G. H. and A. N.; measurement supervision, K. Y. S., and V. N.; writing – original draft preparation, Y. G. H, V. N. ; writing – review and editing, Y. G. H., A. N., V. N., and K. Y. S.; project administration, K. Y. S.; funding acquisition, K. Y. S. and A. N. All authors have read and agree to the published version of the manuscript.

Conflicts of interest

The authors declare that they have no known competing financial interests or personal relationships that could have appeared to influence the work reported in this paper.

Acknowledgements

This work was supported by the National Research Foundation of Korea (NRF) (grants 2021R1I1A1A01061270 and 2021R1I1A3059637), funded by the Ministry of Education.

References

1 J. R. Miller and P. Simon, *Science*, 2008, **321**, 651–652.
2 W. Qi, J. G. Shapter, Q. Wu, T. Yin, G. Gao and D. Cui, *J. Mater. Chem. A*, 2017, **5**, 19521–19540.
3 Y. Zhang, Q. Q. Yao, H. L. Gao, L. X. Wang, L. Z. Wang, A. Q. Zhang, Y. H. Song and T. C. Xia, *Powder Technol.*, 2014, **267**, 268–272.
4 L. Gao, L. Zhang, S. Jia, X. Liu, Y. Wang and S. Xing, *Electrochim. Acta*, 2016, **203**, 59–65.
5 P. Poizot, S. Laruelle, S. Grugeon, L. Dupont and J. M. Tarascon, *Nature*, 2000, **407**, 496–499.
6 X. H. Huang, J. P. Tu, C. Q. Zhang and J. Y. Xiang, *Electrochem. Commun.*, 2007, **9**, 1180–1184.
7 X. Wang, L. Qiao, X. Sun, X. Li, D. Hu, Q. Zhang and D. He, *J. Mater. Chem A*, 2013, **1**, 4173–4176.
8 J. Zhang, D. Zeng, Q. Zhu, J. Wu, Q. Huang and C. Xie, *J. Phys. Chem. C*, 2016, **120**, 3936–3945.
9 J. Liu, S. Du, L. Wei, H. Liu, Y. Tian and Y. Chen, *Mater. Lett.*, 2006, **60**, 3601–3604.
10 C. Li, Y. Liu, L. Li, Z. Du, S. Xu, M. Zhang, X. Yin and T. Wang, *Talanta*, 2008, **77**, 455–459.
11 Z. Cui, H. Yin, Q. Nie, D. Qin, W. Wu and X. He, *J. Electroanal. Chem.*, 2015, **757**, 51–57.
12 X. H. Huang, J. P. Tu, C. Q. Zhang and F. Zhou, *Electrochim. Acta*, 2010, **55**, 8981–8985.
13 W. Yu, X. Jiang, S. Ding and B. Q. Li, *J. Power Sources*, 2014, **256**, 440–448.
14 M. K. Wu, C. Chen, J. J. Zhou, F. Y. Yi, K. Tao and L. Han, *J. Alloys Compd.*, 2018, **734**, 1–8.
15 S. Wang, W. Li, L. Xin, M. Wu, W. Sun and X. Lou, *J. Chem. Eng.*, 2017, **321**, 546–553.
16 D. Xie, W. Yuan, Z. Dong, Q. Su, J. Zhang and G. Du, *Electrochim. Acta*, 2013, **92**, 87–92.
17 V. Aravindan, P. Suresh Kumar, J. Sundaramurthy, W. C. Ling, S. Ramakrishna and S. Madhavi, *J. Power Sources*, 2013, **227**, 284–290.
18 Y. Zou and Y. Wang, *Nanoscale*, 2011, **3**, 2615–2620.
19 L. Liu, Y. Li, S. Yuan, M. Ge, M. Ren, C. Sun and Z. Zhou, *J. Phys. Chem. C*, 2010, **114**, 251–255.
20 W. Liu, C. Lu, X. Wang, K. Liang and B. K. Tay, *J. Mater. Chem. A*, 2015, **3**, 624–633.
21 N. Wang, L. Chen, X. Ma, J. Yue, F. Niu, H. Xu, J. Yang and Y. Qian, *J. Mater. Chem. A*, 2014, **2**, 16847–16850.
22 T. Zhang, F. Zhang, L. Zhang, Y. Lu, Y. Zhang, X. Yang, Y. Ma and Y. Huang, *Carbon*, 2015, **92**, 106–118.
23 S. Sagadevan and J. Podder, *Int. J. Nanoparticles*, 2015, **8**, 289–301.
24 K. Menad, A. Feddag and K. Rubenis, *Rasayan J. Chem.*, 2016, **9**, 788–797.
25 C. H. Wu, S. X. Deng, H. Wang, Y. X. Sun, J. B. Liu and H. Yan, *ACS Appl. Mater. Interfaces*, 2014, **6**, 1106–1112.
26 Q. H. Lu, R. Huang, L. S. Wang, Z. G. Wu, Q. Luo, S. Y. Zuo, J. Li, D. L. Peng, G. L. Han and P. X. Yan, *J. Magn. Magn. Mater.*, 2015, **394**, 253–259.
27 H. Kim, V. Nulu, J. Yoon and W. S. Yoon, *J. Alloys Compd.*, 2019, **778**, 37–46.
28 X. Wang, X. Li, X. Sun, F. Li, Q. Liu, Q. Wang and D. He, *J. Mater. Chem.*, 2011, **21**, 3571–3573.
29 C. Wang, D. Wang, Q. Wang and H. Chen, *J. Power Sources*, 2010, **195**, 7432–7437.
30 T. Li, S. Ni, X. Lv, X. Yang and S. Duan, *J. Alloys Compd.*, 2013, **553**, 167–171.
31 M. C. Biesinger, B. P. Payne, L. W. M. Lau, A. Gerson and R. S. C. Smart, *Surf. Interface Anal.*, 2009, **41**, 324–332.
32 J. S. Moon, A. Nulu, Y. G. Hwang, V. Nulu and K. Y. Sohn, *ChemistrySelect*, 2021, **6**, 7012–7024.
33 H. Liu, G. Wang, J. Liu, S. Qiao and H. Ahn, *J. Mater. Chem.*, 2011, **21**, 3046–3052.
34 A. Nulu, V. Nulu and K. Y. Sohn, *ChemElectroChem*, 2020, **8**, 1259–1269.
35 K. P. C. Yao, D. G. Kwabi, R. A. Quinlan, A. N. Mansour, A. Grimaud, Y. L. Lee, Y. C. Lu and Y. S. Horn, *J. Electrochem. Soc.*, 2013, **160**, 824–831.
36 X. Yu, C. Zhan, R. Lv, Y. Bai, Y. Lin, Z. H. Huang, W. Shen, X. Qiu and F. Kang, *Nano Energy*, 2015, **15**, 43–53.
37 D. Yan, S. H. Li, L. P. Guo, X. L. Dong, Z. Y. Chen and W. C. Li, *ACS Appl. Mater. Interfaces*, 2018, **10**(50), 43946–43952.
38 Q. Wang, X. Jiang, Q. Tong, H. Li, J. Li and W. Yang, *Nanoenergy Adv.*, 2022, **2**(4), 303–315.
39 Y. Kado, Y. Soneda, H. Hatori and M. Kodama, *J. Solid State Electrochem.*, 2019, **23**, 1061–1081.
40 E. R. Pinero, K. Kierzek, J. Machnikowski and F. Béguin, *Carbon*, 2006, **44**, 2498–2507.
41 D. Puthusseri, V. Aravindan, S. Madhavi and S. Ogale, *Electrochim. Acta*, 2014, **130**, 766–770.
42 W. J. Cao and J. P. Zheng, *J. Power Sources*, 2012, **213**, 180–185.
43 Y. Zhao, Y. Cui, J. Shi, W. Liu, Z. Shi, S. Chen, X. Wang and H. Wang, *J. Mater. Chem. A*, 2017, **5**, 15243–15252.
44 J. H. Kim, J. S. Kim, Y. G. Lim, J. G. Lee and Y. J. Kim, *J. Power Sources*, 2011, **196**, 10490–10495.
45 X. Sun, X. Zhang, W. Liu, K. Wang, C. Li, Z. Li and Y. Ma, *Electrochim. Acta*, 2017, **235**, 158–166.
46 H. G. Jung, N. Venugopal, B. Scrosati and Y. K. Sun, *J. Power Sources*, 2013, **221**, 266–271.
47 F. Zhang, T. Zhang, X. Yang, L. Zhang, K. Leng, Y. Huang and Y. Chen, *Energy Environ. Sci.*, 2013, **6**, 1623–1632.
48 X. L. Wu, L. L. Jiang, C. L. Long, T. Wei and Z. J. Fan, *Adv. Funct. Mater.*, 2015, **25**, 1648–1655.
49 H. Xia, C. Y. Hong, B. Li, B. Zhao, Z. X. Lin, M. B. Zheng, S. V. Savilov and S. M. Aldoshin, *Adv. Funct. Mater.*, 2015, **25**, 627–635.